

Cracking Potential of Alkali-Activated Concrete Induced by Autogenous Shrinkage

Li, Zhenming; Zhang, Shizhe; Liang, Xuhui; Kostiuhenko, Albina; Ye, Guang

DOI

[10.1007/978-3-030-76551-4_22](https://doi.org/10.1007/978-3-030-76551-4_22)

Publication date

2021

Document Version

Accepted author manuscript

Published in

Proceedings of the 3rd RILEM Spring Convention and Conference (RSCC 2020)

Citation (APA)

Li, Z., Zhang, S., Liang, X., Kostiuhenko, A., & Ye, G. (2021). Cracking Potential of Alkali-Activated Concrete Induced by Autogenous Shrinkage. In I. B. Valente (Ed.), *Proceedings of the 3rd RILEM Spring Convention and Conference (RSCC 2020)* (pp. 239-245). (RILEM Bookseries; Vol. 33). Springer. https://doi.org/10.1007/978-3-030-76551-4_22

Important note

To cite this publication, please use the final published version (if applicable).
Please check the document version above.

Copyright

Other than for strictly personal use, it is not permitted to download, forward or distribute the text or part of it, without the consent of the author(s) and/or copyright holder(s), unless the work is under an open content license such as Creative Commons.

Takedown policy

Please contact us and provide details if you believe this document breaches copyrights.
We will remove access to the work immediately and investigate your claim.

Cracking potential of alkali-activated slag and fly ash concrete subjected to restrained autogenous shrinkage

Zhenming Li^{a,*}, Shizhe Zhang^a, Xuhui Liang^a, Guang Ye^{a,b}

^aDepartment of Materials and Environment (Microlab), Faculty of Civil Engineering and Geoscience, Delft University of Technology, Delft, the Netherlands

^bMagnel Laboratory for Concrete Research, Department of Structural Engineering, Ghent University, Ghent, Belgium

Abstract

This study aims to investigate the cracking potential of alkali-activated slag (AAS) and alkali-activated slag-fly ash (AASF) concrete subjected to restrained autogenous shrinkage. Temperature Stress Testing Machine (TSTM) is utilized, for the first time, to monitor the stress evolution and to measure the cracking time of alkali-activated concrete (AAC) under restraint condition. The stresses in AAS and AASF concrete are calculated based on the experimental results while taking into consideration the influence brought by creep and relaxation. It is found that AAS and AASF concrete showed lower autogenous shrinkage-induced stress and later cracking compared to ordinary Portland cement (OPC) based concrete with similar compressive strength, despite the higher autogenous shrinkage of AAS and AASF concrete. The low autogenous shrinkage-induced stress in the AAC is mainly attributed to the pronounced stress relaxation. A good prediction of the stress evolution in AAC is obtained by taking into account the elastic part of the autogenous shrinkage and the stress relaxation. In contrast, calculations ignoring the creep and relaxation would lead to a significant overestimation of the stress in AAC.

Keywords: cracking, shrinkage, stress, alkali-activated materials, concrete, modelling

1. Introduction

Alkali-activated materials (AAMs) have emerged as eco-friendly alternatives to OPC as binder materials in engineering practice [1]. In comparison to OPC, AAMs can significantly reduce the environmental impacts of concrete products by lowering greenhouse gas emissions and the embodied energy [2]. Furthermore, using AAMs as binders could also contribute to the repurposing of industrial by-products [3,4].

Currently, granulated blast-furnace slag (hereinafter termed slag) and powered coal fly ash (hereinafter termed fly ash) are the two most widely utilized precursors for AAMs. Among two types of fly ash, namely Class C and Class F fly ash according to ASTM C618 [5], Class F fly ash with reactive $\text{CaO} \leq 10\%$ has been intensively studied worldwide due to its wide availability and high content of amorphous aluminosilicate phases [6]. Alkali activator is usually an alkali metal hydroxide and/or silicate [7]. Although Na_2CO_3 and Na_2SO_4 can also be used as activators [8,9], the majority of studies have shown that activation with Na_2SiO_3 and/or NaOH provides high mechanical properties for slag and fly ash-based AAMs [10]. NaOH activators

39 are found to accelerate early-age activation but tend to present a barrier to advanced
40 reactions, therefore limiting the later-age strength [11]. In contrast, the reaction of Na_2SiO_3 -
41 activated slag is comparatively slow and results in the formation of very dense products with
42 improved mechanical strength [12].

43 Despite the promising mechanical and eco-friendly performance, slag and fly ash-based AAMs
44 have not received broad industry acceptance, primarily due to the uncertain long-term
45 durability and volume stability [13–15]. As reported in [16–25], slag and fly ash-based AAMs,
46 especially those activated by $\text{NaOH}/\text{Na}_2\text{SiO}_3$, can show higher autogenous shrinkage than OPC
47 based systems. The high autogenous shrinkage of AAMs is concerned by both academia and
48 industrial communities because it can potentially induce cracking of concrete [26,27]. In
49 practice, concrete as building material is normally applied under restrained conditions. The
50 restraint can be either external (e.g. caused by adjoining structure) or internal (e.g., caused by
51 the reinforcement or the non-shrinking aggregates) to the concrete member [28–30]. The
52 volume change of the concrete would be therefore limited to a certain extent and
53 consequently internal tensile stress would develop. Cracking would occur when the tensile
54 stress within concrete exceeds the tensile strength, which can lead to a series of problems
55 regarding mechanical properties, durability and aesthetics of concrete structures [31].
56 Therefore, the cracking potential of activated slag and fly ash concrete has to be evaluated to
57 provide a solid theoretical basis for safe and reliable application of these materials.

58 From the high autogenous shrinkage of alkali-activated slag and fly ash systems, one may
59 deduce that AAC will show higher cracking potential compared to OPC based concrete.
60 However, the cracking potential of concrete is determined not only by autogenous shrinkage
61 but also by elastic modulus, creep/relaxation and tensile strength of the material. However,
62 very few studies on this topic can be found from the literature [32].

63 The aim of this study, therefore, is to evaluate the autogenous shrinkage-induced cracking
64 potential of AAS and AASF concrete. Temperature Stress Testing Machine (TSTM) is utilized to
65 track the internal stress evolution and cracking initiation of the concrete under restraint
66 condition. With the measured autogenous shrinkage and elastic modulus as inputs, the
67 internal stresses in AAS and AASF concrete are calculated and compared with the
68 experimental results. The roles of creep and relaxation in influencing the stress evolution and
69 cracking potential of AAC are highlighted.

70 **2. Materials and methods**

71 **2.1 Raw materials and mixtures**

72 The precursors used were slag supplied by Ecocem Benelux B.V and fly ash from Vliegasonie
73 B.V. The chemical compositions of slag and fly ash were determined by X-ray fluorescence (XRF)
74 and shown in Table 1. The fly ash complies with Class F (EN 450, ASTM C618) since it has low
75 CaO content (< 10% reactive CaO) and content of " $\text{SiO}_2 + \text{Al}_2\text{O}_3 + \text{Fe}_2\text{O}_3$ " higher than 70%. The
76 particle size of slag, as measured by laser diffraction, ranges from 0.1 to 50 μm , with a d_{50} of
77 18.3 μm . The particle size of fly ash is between 0.14 and 138 μm , with a d_{50} of 48.1 μm .

78

79

80 Table 1. Chemical propositions of slag and fly ash.

Oxide (wt. %)	SiO ₂	Al ₂ O ₃	CaO	MgO	Fe ₂ O ₃	SO ₃	K ₂ O	TiO ₂	Other	LOI
Slag	31.77	13.25	40.50	9.27	0.52	1.49	0.34	0.97	0.21	1.31
Fly ash	56.8	23.8	4.8	1.5	7.2	0.3	1.6	1.2	1.6	1.2

81 LOI= Loss on ignition

82

83 The alkaline activator was prepared by mixing anhydrous pellets of sodium hydroxide with
 84 deionized water and commercial sodium silicate solution. For 1000 g of precursor, an activator
 85 containing 384 g of water, 1.146 mol of SiO₂ and 0.76 mol of Na₂O was applied. The water-to-
 86 solid ratio is therefore 0.344 if the alkali in the activator is considered as solid. The activator
 87 was prepared at least one day before the casting of the concrete so that the solution was
 88 cooled down to ambient temperature.

89 The concrete mixture designs are shown in Table 2.

90

91 Table 2. Mixture design of AAS and AASF concrete (kg/m³).

Mixtures	AAS	AASF
Slag	400	200
Fly ash	0	200
Activator	200	200
Aggregate [0-4 mm]	789	789
Aggregate [4-8 mm]	440	440
Aggregate [8-16 mm]	525	525
Admixtures	-	-

92

93

94 2.2 Experimental methods

95 2.2.1 Mechanical properties

96 Concrete cubes (150 × 150 × 150 mm³) for compressive and splitting strength tests and prisms
 97 (100 × 100 × 400 mm³) for elastic modulus test were cast and cured in sealed and temperature-
 98 controlled steel moulds. The moulds were connected with cryostats by parallel circulation
 99 tubes and the upper surface was sealed by plastic film. The temperature of the concrete cubes
 100 was controlled at 20 °C.

101 Compressive strength and splitting strength of the concrete were measured according to NEN-
 102 EN 12390 [33]. The measurements were conducted at the age of 1, 3, 7, 28 days and the day
 103 when the beam in TSTM cracked. One cube was tested for compressive strength and two for
 104 splitting strength.

105 The elastic modulus of the concrete was tested by a Tonibank hydraulic Instron (Figure 1). The
106 strain during loading was measured by linear variable differential transducers (LVDTs) aligned
107 vertically on the four sides of the concrete prism. The loading and unloading of each sample
108 went through four cycles with the stress ranging from 5% to 30% of the compressive strength
109 of the concrete. The results obtained from the latter three cycles were used in the calculation
110 of the elastic modulus. The loading and unloading rates were 1 kN/s [34]. Two samples were
111 tested for each mixture at each age.



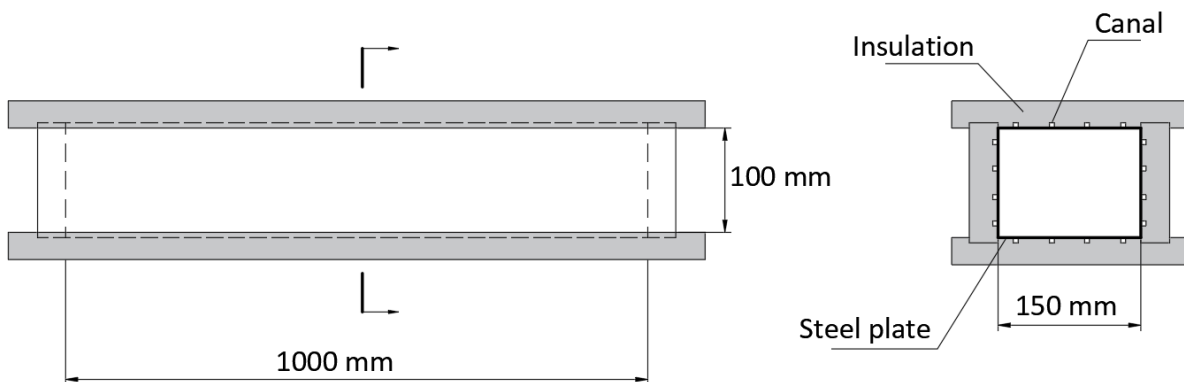
112

113 Figure 1. Testing set-up for elastic modulus measurement on AAC.

114

115 2.2.2 Autogenous shrinkage

116 The autogenous shrinkage of the concrete was measured with an Autogenous Deformation
117 Testing Machine (ADTM) [35]. The prismatic mould for the concrete is made of thin steel
118 plates and external insulating materials. The size of the mould is $1000 \times 150 \times 100 \text{ mm}^3$, which
119 is illustrated in Figure 2. The mould was connected with cryostats by a series of circulation
120 tubes located between the plates and the insulating material (see Figure 2). The temperature
121 of the beam was controlled at $20 \text{ }^\circ\text{C}$.

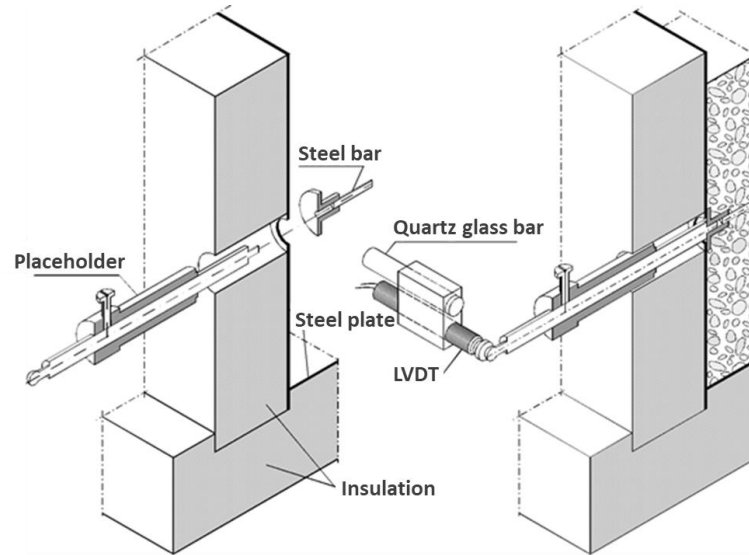


122

123 Figure 2. Front view (left) and cutaway view (right) of the mould of Autogenous Deformation Testing Machine
124 (ADTM).

125

126 The length change of the concrete was measured with two external quartz rods located next
127 to the side mould. LVDTs were installed at both ends of the rods. The LVDTs measured the
128 movement of the steel bars which were cast in the concrete. The distance between the two
129 cast-in steel bars was 750 mm. The instalment of LVDTs was conducted only when the
130 concrete had reached sufficient strength to support them (see Figure 3). The measurement of
131 the deformation of AAS and AASF concrete starts at 8h and 11h, respectively. Attention was
132 paid to the sealing of the moulds in order to avoid moisture loss to the environment.



133

134 Figure 3. Installation of measuring bars and placeholders before casting (left) and installation of LVDTs when
135 the concrete is stiff enough to support the bars (right), after [35].

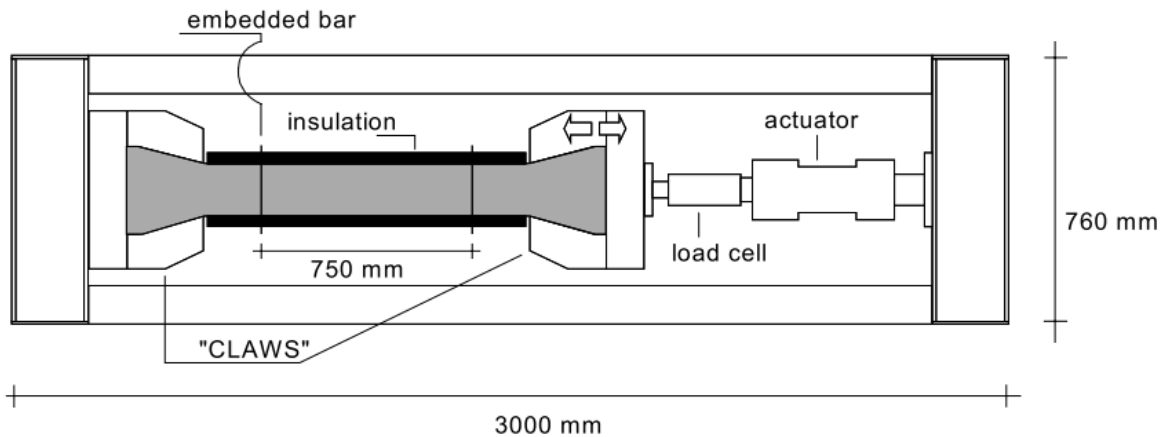
136

137 2.2.3 Autogenous shrinkage-induced stress

138 The internal tensile stress in the concrete induced by restrained autogenous shrinkage was
139 monitored by TSTM. A sudden drop of the stress indicated the occurrence of cracking. The
140 TSTM was equipped with a horizontal steel frame (Figure 4) in which the concrete specimen
141 can be loaded in compression or in tension under various temperatures. The whole specimen
142 is of a dog-bone shape and the testing area of interest is of prismatic shape ($1000 \times 150 \times 100$
143 mm^3). The middle part of the specimen is in a temperature-controlled mould, similar to the
144 ADTM mould as described in Section 2.2.2. Two rigid steel claws were used to grip the
145 concrete specimen. One of the claws was fixed to the steel frame while the other one lied on
146 roller bearings and thereby can move with the hydraulic actuator to provide a compressive or
147 tensile force onto the testing specimen. A short formwork was attached to the claws to
148 provide a smooth and curved transition between the straight insulated mould and the slanting
149 inner sides of the claws. The load was recorded with the load-cell with a loading capacity of
150 100 kN and a resolution of 0.049 kN.

151 During the first 8 hours after casting, LVDTs were used to control the deformation between
152 the two claws because it was not yet possible to measure the deformations of the fresh
153 concrete with the embedded steel bars. After that, the deformation control was switched to
154 the LVDTs that measure the displacement between the embedded bars. The deformation of

155 the concrete was kept at zero (nominally, in reality within 1 μm range) so that a full restraint
 156 condition was provided.



157

158 Figure 4. Top view of the Temperature Stress Testing Machine (TSTM) [36].

159 2.3 Calculation of the autogenous shrinkage-induced stress

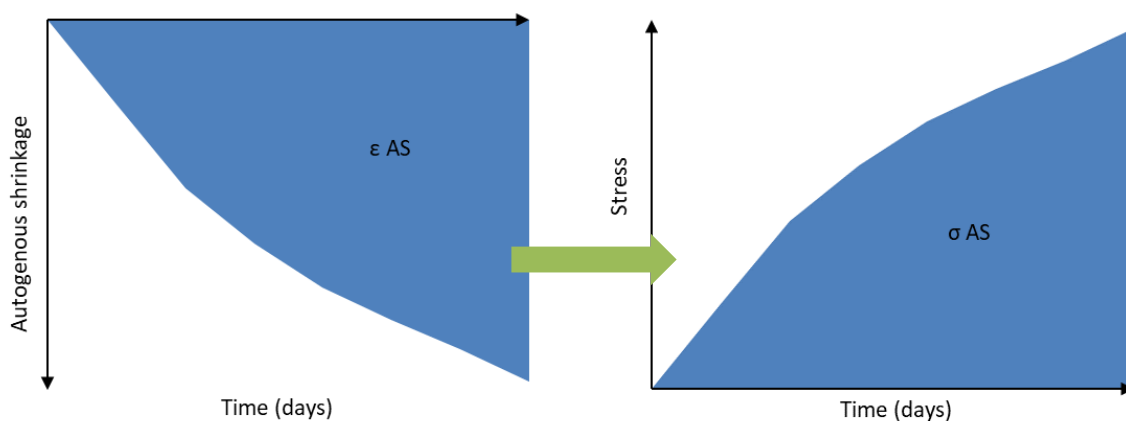
160 While the autogenous shrinkage-induced stress in restrained concrete can be monitored by
 161 TSTM, the test is very time-consuming and labour-intensive. Besides, TSTM is currently not
 162 equipped widely enough to serve as a standard apparatus. Therefore, it would be meaningful
 163 if the stress evolution can be predicted based on the experimental results obtained in concrete
 164 under free conditions.

165 2.3.1 Calculation of the stress based on autogenous shrinkage

166 If the autogenous shrinkage is assumed to be purely elastic deformation [29], the stress (σ_{AS})
 167 generated in the concrete due to restrained shrinkage can be calculated using Equation 1. A
 168 schematic representation of the calculation process is shown in Figure 5.

$$169 \sigma_{AS} = \varepsilon_{AS} \times E \quad (1)$$

170 where ε_{AS} is the measured autogenous shrinkage of the concrete and E is the measured
 171 elastic modulus of the concrete.



172

173 Figure 5. Schematic representation of stress calculated based on autogenous shrinkage.

174 **2.3.2 Calculation of the stress based on the elastic part of the autogenous shrinkage**

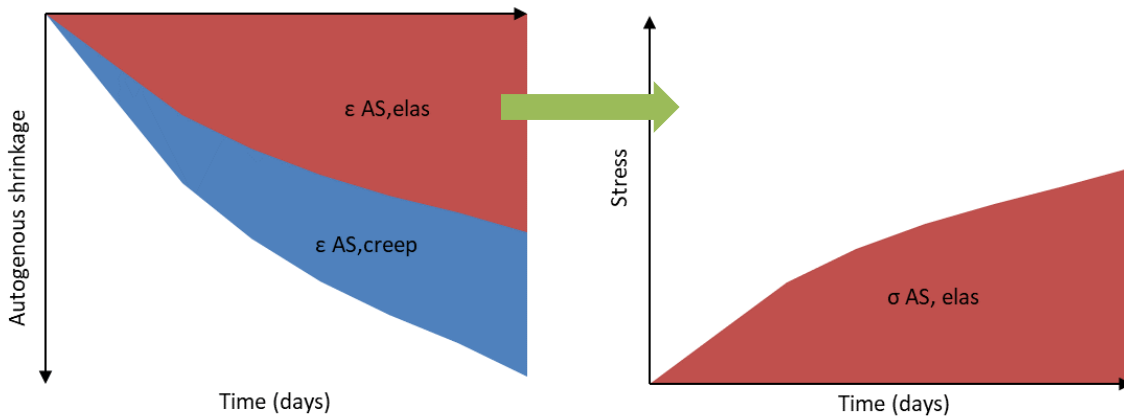
175 In fact, the concrete, either OPC based concrete or AAC, is not a purely elastic material [26,37].
 176 Under external or internal load, the concrete tends to generate time-dependent deformation,
 177 or so-called creep, due to the viscoelasticity of the material. Therefore, a part of the
 178 autogenous shrinkage of the concrete measured under free condition actually belongs to
 179 creep deformation [38]. When the concrete is under externally restrained condition, the creep
 180 part of the autogenous shrinkage does not have the potential to develop due to the
 181 equilibrium between the internal driving force and the external restraint force. Therefore, the
 182 stress in the restrained concrete is predominantly caused by the elastic part of the autogenous
 183 shrinkage [39]. If we assume the stress in the concrete is solely induced by the elastic part of
 184 the autogenous shrinkage and do not consider the stress relaxation, the stress can be
 185 calculated using Equations 2 and 3. A schematic representation of the calculation process is
 186 shown in Figure 6.

187
$$\epsilon_{AS} = \epsilon_{AS,elas} + \epsilon_{AS,creep} \quad (2)$$

188 where ϵ_{AS} is the measured autogenous shrinkage of AAC. $\epsilon_{AS,elas}$ and $\epsilon_{AS,creep}$ are the elastic
 189 part and creep part of the autogenous shrinkage of AAC, respectively.

190
$$\sigma_{AS,elas} = \epsilon_{AS,elas} \times E \quad (3)$$

191 where $\sigma_{AS,elas}$ is the stress induced by the elastic part of the autogenous shrinkage ($\epsilon_{AS,elas}$).



192
 193 Figure 6. Schematic representation of stress calculated based on the elastic part of the autogenous shrinkage.

194
 195 The relationship between the creep deformation and the elastic deformation under a load can
 196 be expressed by Equation 4 [26,40].

197
$$\epsilon_{AS,creep}(t, \tau) = \epsilon_{AS,elas}(\tau)\varphi(t, \tau) \quad (4)$$

198 where $\varphi(t, \tau)$ is the creep coefficient. τ (days) is the time when the load is applied.

199 According to [39,41], the creep coefficient of OPC based concrete can be calculated by
 200 Equation 5. For AAC systems, however, no models are available yet to account for the creep

201 deformation. Therefore, Equation 5 is tentatively used in this study to calculate the creep
 202 coefficient of AAC.

$$203 \quad \varphi(t, \tau) = \left(\frac{\alpha(t)}{\alpha(\tau)} - 1 \right) + 1.34 * \omega^{1.65} \tau^{-d} (t - \tau)^n \frac{\alpha(t)}{\alpha(\tau)} \quad (5)$$

204 where α is the degree of reaction. ω is the water-to-solid ratio (0.344, see section 2.1). n is
 205 the relaxation factor whose value is empirically taken as 0.3 and d is the constant whose value
 206 is empirically taken as 0.35 according to [41].

207 The reaction degree α of the concrete can be calculated with Equation 6 [42–44].

$$208 \quad \alpha(t) = \frac{Q(t)}{Q_{max}} \quad (6)$$

209 where $Q(t)$ is the reaction heat and Q_{max} is the ultimate total heat at the completion of the
 210 reaction. $Q(t)$ and Q_{max} of AAC are calculated according to the procedure described in
 211 Appendix A.

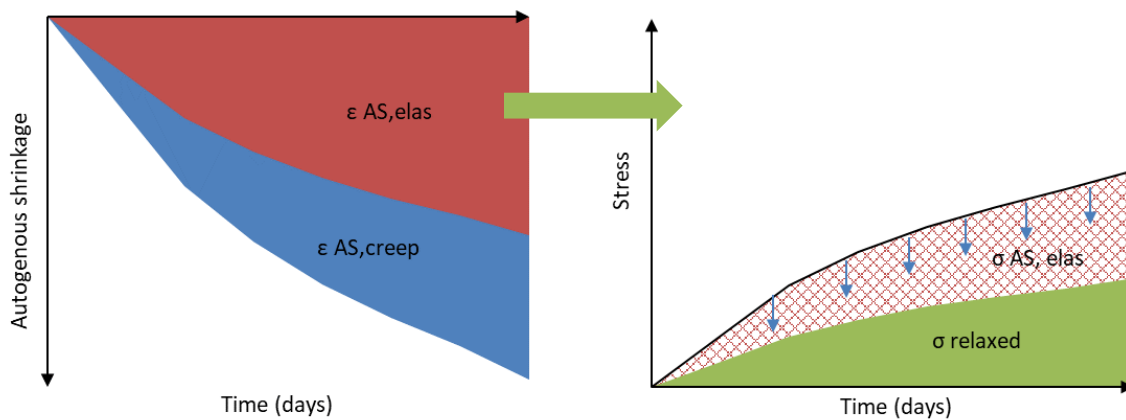
212 With Equations 2 and 4– 6, the elastic part and creep part of the autogenous shrinkage of AAC
 213 can be calculated.

214 2.3.3 Calculation of the stress by taking relaxation into account

215 Like the creep of the concrete under free condition, stress relaxation in concrete under
 216 restrained condition is another result of the viscoelasticity of the material. Due to the
 217 relaxation, the stress generated in restrained concrete would be reduced with the elapse of
 218 time. According to van Breugel [39], the stress induced by restrained elastic deformation can
 219 be calculated with Equation 7 by taking into consideration of the relaxation. A schematic
 220 representation of the calculation process of the stress induced by restrained autogenous
 221 shrinkage is shown in Figure 7.

$$222 \quad \sigma_{relaxed}(t, \tau) = \sigma_{elas}(\tau) \psi(t, \tau) \quad (7)$$

223 where $\psi(t, \tau)$ is the relaxation factor. τ (days) is the time when the load is applied.



224

225 Figure 7. Schematic representation of stress calculated based on the elastic part of the autogenous shrinkage by
 226 taking relaxation into account.

227 The relaxation coefficient of concrete can be calculated from the creep coefficient $\varphi(t, \tau)$
 228 using Equation 8 [39,45].

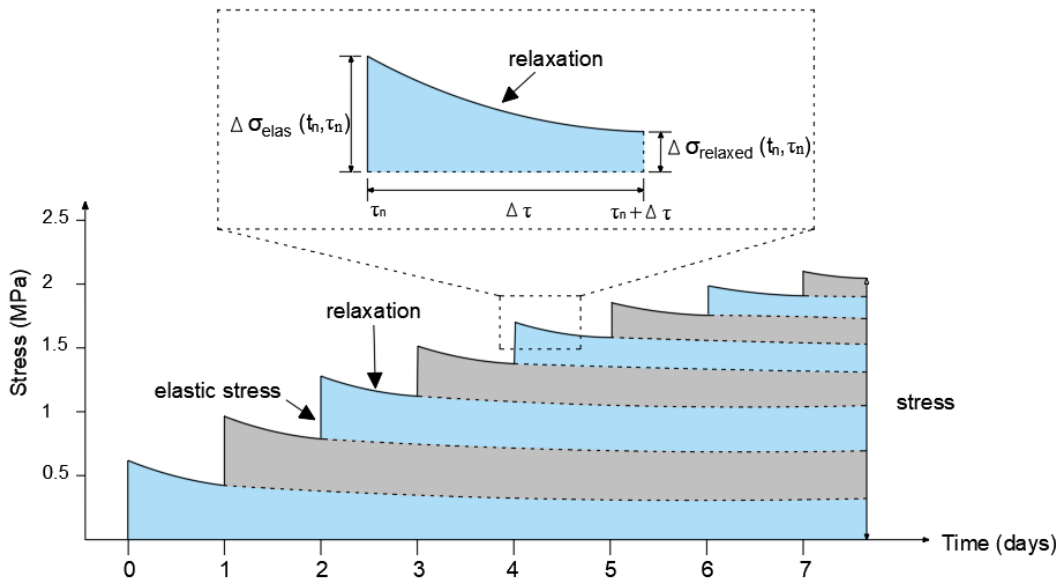
$$229 \quad \psi(t, \tau) = e^{-\varphi(t, \tau)} \quad (8)$$

230 The stress generated in the concrete after a certain curing age can be considered as the
 231 accumulations of the stresses resulting from the elastic deformations that occurred at
 232 previous time intervals, e.g. from τ_1 to τ_{n-1} , as shown in Equation 9.

$$233 \quad \sigma_{relaxed} = \sum_{k=1}^{n-1} \Delta\sigma_{relaxed}(\tau_k) \quad (9)$$

234 where $\Delta\sigma_{relaxed}(t_k, \tau_k)$ is the increment of elastic shrinkage-induced stress after relaxation
 235 from τ_k to τ_{k+1} .

236 A schematic representation of the calculation process mentioned above is shown in Figure 8.



237

238

Figure 8. Schematic representation of stress generated in concrete.

239

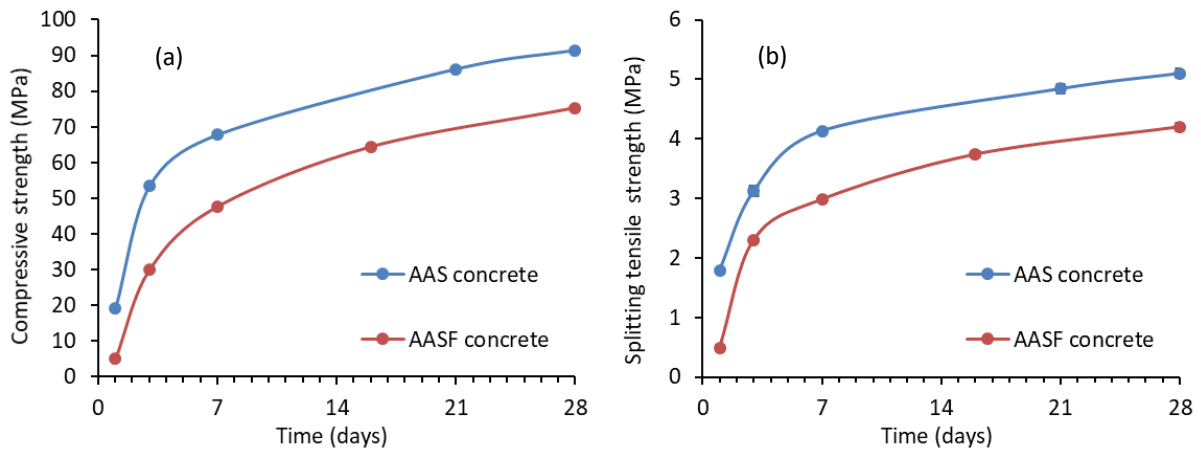
240 3. Experimental results and discussion

241 3.1 Mechanical properties

242 3.1.1 Compressive and splitting tensile strength

243 The strength development of the concrete is shown in Figure 9. It can be seen that AAC
 244 generally shows high strength. At the age of 28 days, the compressive strength of AAS and
 245 AASF concretes is around 90 MPa and 75 MPa, respectively. According to EN 206 [46], the
 246 strength can be classified as C60 or higher. AAS concrete shows higher compressive and
 247 splitting strength than AASF concrete, which is consistent with the findings on the positive
 248 correlation between slag/fly ash ratio and the mechanical properties in the literature [47–49].
 249 The lower strength of AASF concrete is due to the replacement of slag by fly ash, which has a

250 low reactivity at ambient temperature [50]. The dissolution of fly ash particles is slow no
 251 matter in cementitious systems or in alkali-activated systems [50,51]. Nonetheless, with the
 252 elapse of time the amorphous phases in fly ash would eventually contribute to the strength
 253 growth [51], which can be reflected by the considerable increase of the compressive strength
 254 of AASF concrete from 7 days to 28 days.



255

256 Figure 9. Compressive (a) and splitting strength (b) of AAC. For the splitting strength, the error bar is shown in
 257 the diagram, but it is too small to be clearly distinguished from the marker.

258

259 Despite the high compressive strength of AAC mixtures, their splitting tensile strength is not
 260 remarkably high. This can be seen more clearly in Figure 10, in which the splitting tensile
 261 strength -to-compressive strength ($f_{t,sp}/f_c$) ratios of the concrete are plotted. The $f_{t,sp}/f_c$ ratio
 262 is an important parameter that allows the estimation of $f_{t,sp}$ by knowing f_c or vice versa [52].
 263 The ratio also provides insight into the stress type (compression or tension) to which the
 264 concrete is more prone. It can be seen from Figure 10 that AAS and AASF concretes showed
 265 nearly identical $f_{t,sp}/f_c$ except at the age 3 days.

266 The $f_{t,sp}/f_c$ ratio of AAC decreases from around 0.1 at the first day to only 0.055 at 28 days. This
 267 decrease might be due to the development of microcracking within the concrete resulting
 268 from the restrained autogenous shrinkage of the material [53,54]. Although the samples for
 269 strength test were not subject to external restraint, the aggregates can act as local restraints
 270 to the autogenous shrinkage of the surrounding paste [55]. Due to the large autogenous
 271 shrinkage of AAC (as will be discussed in the following section), microcracks may have
 272 developed within the concrete, although no visual cracks were observed on the surface of the
 273 sample. The development of microcracking can harm the increase of tensile strength.
 274 Although the absolute tensile strength of AAC increased with the curing age as shown in Figure
 275 9, the developing rate of the tensile strength became lower than that of the compressive
 276 strength as indicated by the decreasing $f_{t,sp}/f_c$.

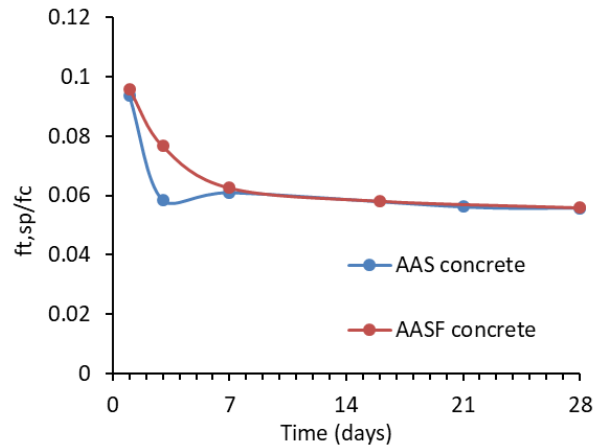


Figure 10. Splitting tensile strength-to-compressive strength ($f_{t,sp}/f_c$) ratios of AAC.

277

278

279

280 3.1.2 Elastic modulus

281 The elastic modulus of AAC is shown in Figure 11. AAS concrete showed higher elastic modulus
 282 than AASF concrete at the early age. After 7 days, however, the elastic modulus of AAS
 283 concrete started to decrease slightly while the one of AASF concrete kept increasing. At 28
 284 days, AAS and AASF concrete showed similar elastic modulus.

285 The decline of elastic modulus of AAS concrete with curing age has also been reported by
 286 Prinsse et al. [54], in which both reduced elastic modulus and splitting tensile strength were
 287 observed in AAS concrete. In that study, the concrete was cured in a climate chamber with the
 288 temperature at 20°C and the relative humidity above 95%, after demoulded at 1 day. The
 289 reduction was attributed to the leaching of ions from the sample and the change of curing
 290 condition when the samples were taken out from the climate chamber to ambient condition
 291 for testing [54]. The loss of structural ions due to leaching and the severe drop of the
 292 environment relative humidity from above 95% to around 50% may induce substantial drying
 293 shrinkage and related microcracking, thus damaging the microstructure of the concrete [56].
 294 This study, in contrast, applied sealed curing before the samples were tested in ambient
 295 relative humidity. Therefore, no leaching occurred. The change of the environment RH and
 296 the impact on the consequent drying shrinkage should be much less severe than that reported
 297 in [54]. However, the autogenous shrinkage, as will be discussed in the coming section, had
 298 already been developing before the exposure of the samples for strength tests, which can also
 299 induce microcracking. Therefore, the reduced elastic modulus of AAS concrete herein is
 300 believed to be due to the same reason for the reduced $f_{t,sp}/f_c$ of the concrete, which is the
 301 development of microcracking caused by autogenous shrinkage.

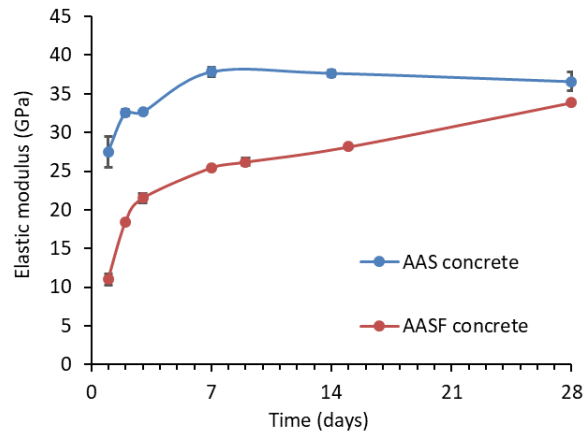


Figure 11. Elastic modulus of AAC.

302

303

304

305 3.2 Autogenous shrinkage

306 The autogenous shrinkage of the concrete is shown in Figure 12. AASF concrete showed lower
 307 autogenous shrinkage than AAS concrete in the whole period studied. This findings are
 308 consistent with the autogenous shrinkage results on corresponding AAS and AASF pastes [37].
 309 The autogenous shrinkage of AAS and AASF concrete develops rapidly at the first day and
 310 second day, respectively, which are in line with the accelerated reaction stages of the mixtures
 311 (see Figure A.1). At the age of 21 days, the autogenous shrinkage of AAS and AASF concrete
 312 reaches 609 and 325 $\mu\text{m}/\text{m}$, respectively.

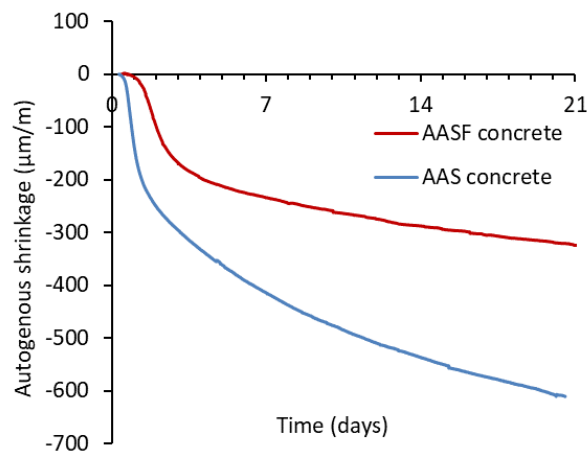


Figure 12. Autogenous shrinkage of AAC obtained from ADTM measurements.

313

314

315

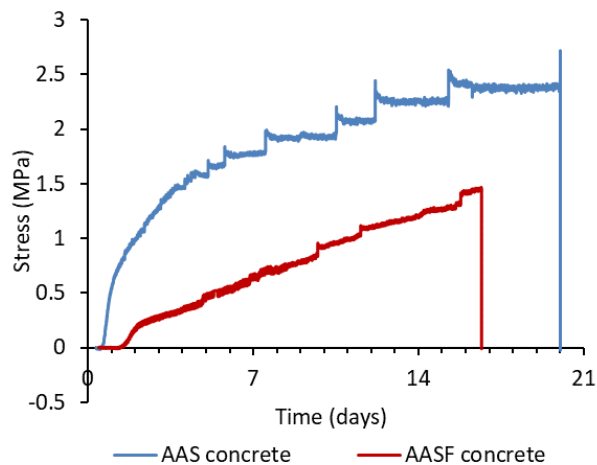
316 3.3 Autogenous shrinkage-induced stress

317 Figure 13 shows the stress development in AAS and AASF concrete tested by TSTM. The
 318 sudden drop in the stress to around zero indicates the occurrence of cracking in concrete. It
 319 can be seen that AAS concrete showed a rapid stress development due to the high autogenous
 320 shrinkage. The stress in AASF concrete remains low in the first 1.5 days due to low shrinkage

321 (see Figure 12). The tensile stress generated in AASF concrete was substantially lower than in
 322 AAS concrete. The lower autogenous shrinkage and also the lower elastic modulus of AASF
 323 concrete contribute to the lower stress in AASF concrete than in AAS concrete. Nonetheless,
 324 the tensile strength (1.4 MPa) tested by TSTM of AASF concrete was also lower than that of
 325 AAS concrete (2.7 MPa). Eventually, AASF concrete cracked even earlier than AAS concrete.

326 The classification of cracking potential according to ASTM C1581 [36] is shown in Table 3,
 327 where cracking time (in days) and average stress rate (in MPa/day) were considered.
 328 Accordingly, the cracking potential of the two concrete mixtures belongs to the category
 329 “moderate-low”. Compared with the results obtained by TSTM on OPC based concrete in the
 330 literature [31,57,58], it can be seen that AAC showed lower stress and later cracking than OPC
 331 based concrete with similar strength. The lower cracking potential of AAC than OPC based
 332 concrete with similar or even lower strength is very positive information for the application of
 333 AAC as a building material.

334 The reason why AAC showed higher autogenous shrinkage but later cracking initiation than
 335 OPC based concrete is believed to be mainly due to the stress relaxation. The evident
 336 relaxation of AAC is in line with the large creep of AAM paste identified in [59,60]. These two
 337 phenomena, creep and relaxation, both originate from the viscoelasticity of the material [61].
 338 In the next section, the creep part of the autogenous shrinkage will be quantified.



339
 340 Figure 13. Autogenous shrinkage-induced stress in AAC obtained by TSTM measurements.

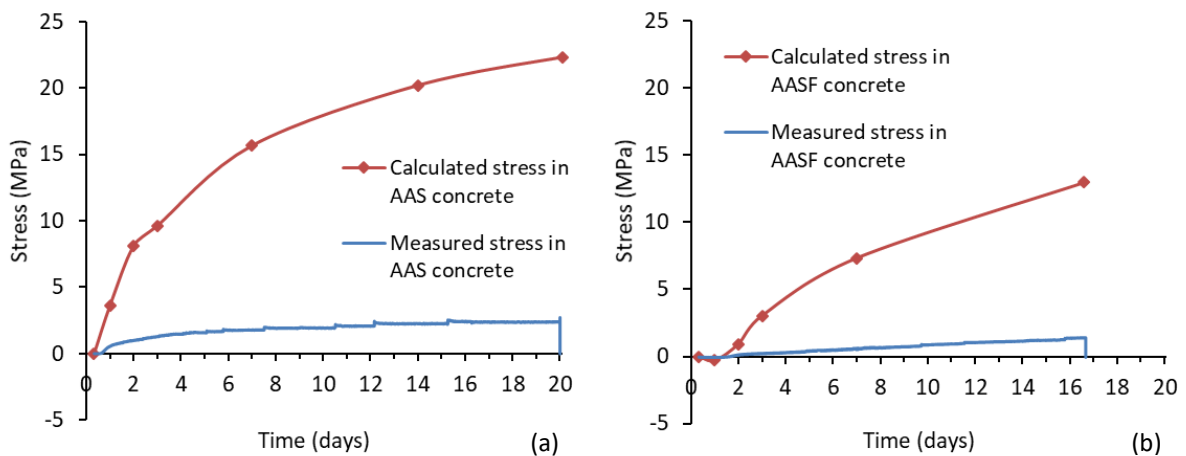
341
 342 Table 3. Classification of cracking potential according to ASTM C1581 [36].

Cracking time t_{cr} (days)	Average stress rate S (MPa/day)	Potential for cracking
$0 < t_{cr} \leq 7$	$S \geq 0.34$	High
$7 < t_{cr} \leq 14$	$0.17 \leq S < 0.34$	Moderate-High
$14 < t_{cr} \leq 28$	$0.10 \leq S < 0.17$	Moderate-Low
$t_{cr} > 28$	$S < 0.10$	Low

344 **4. Numerical results and discussion**

345 **4.1 Calculated stress based on autogenous shrinkage**

346 The calculated stress with Equation 1, based on the autogenous shrinkage (see Figure 12) and
347 the elastic modulus (see Figure 11) of the concrete, are presented and compared with
348 measured stress in Figure 14. It can be seen that the calculated stress in AAC is around 7-8
349 times higher than the experimentally measured one. These results confirm that the
350 creep/relaxation plays an important role in the stress development in AAC. The stress is
351 significantly overestimated when the creep part in the autogenous shrinkage and the stress
352 relaxation are not considered.

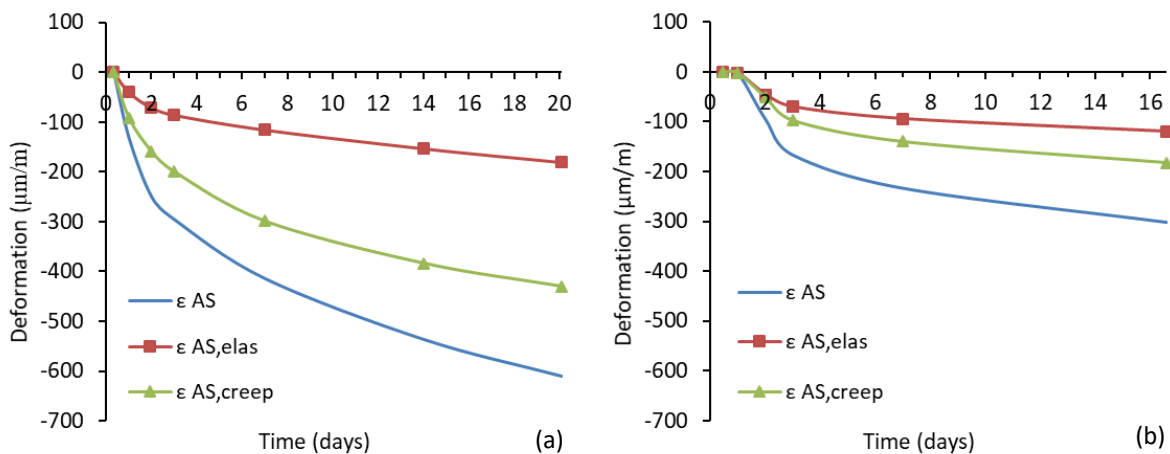


353

354 Figure 14. Calculated stress in AAS (a) and AASF (b) concrete from the autogenous shrinkage and the elastic
355 modulus of the concrete.

356 **4.2 Calculated stress based on the elastic part of autogenous shrinkage**

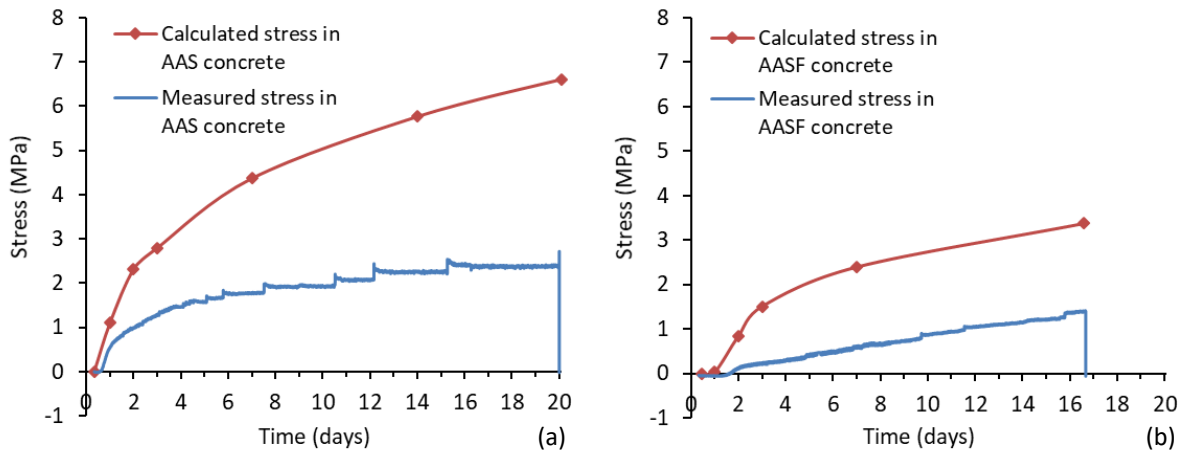
357 According to Equations 2 and 4 – 6, the elastic part and creep part of the autogenous shrinkage
358 of AAC can be calculated, as shown in Figure 15.



359

360 Figure 15. Calculated elastic part and creep part of autogenous shrinkage of AAS (a) and AASF (b) concrete. The
361 autogenous deformation curve for AASF concrete is modified during modelling in order to exclude the
362 influence of expansion

363 The calculated stress in AAC according to Equation 3 is shown in Figure 16. It can be seen that
 364 considering only the elastic part of autogenous shrinkage in calculation gives a much better
 365 prediction of the shrinkage-induced stress than the results shown in Figure 14, where the total
 366 autogenous shrinkage was used as input. Nonetheless, the calculated stress is still two times
 367 higher than the stress measured by TSTM, indicating that the relaxation of the stress has to
 368 be considered in order to estimate the time-dependent stress.



369

370 Figure 16. Calculated stress in AAS (a) and AASF (b) concrete from the elastic part of the autogenous shrinkage
 371 and the elastic modulus of the concrete.

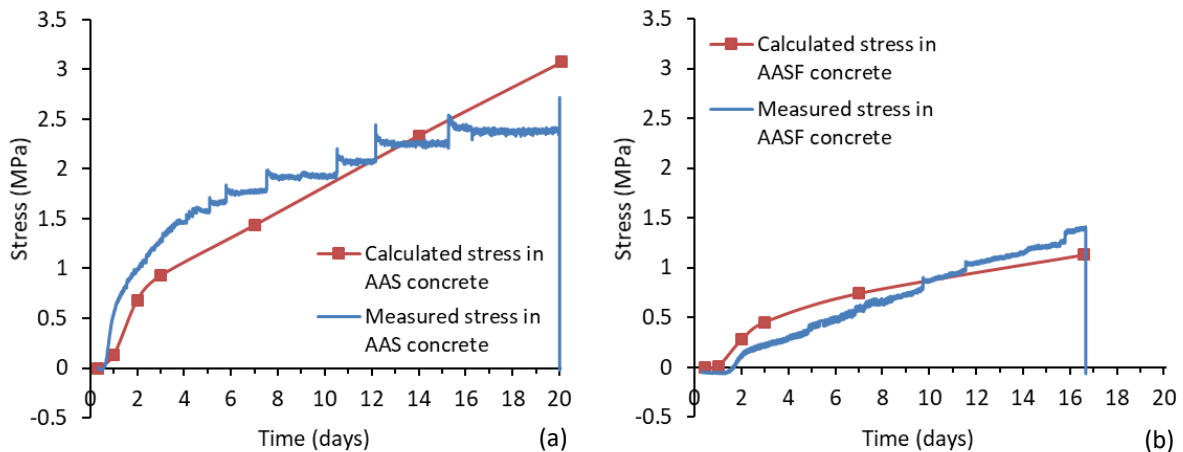
372

373 4.3 Calculated stress by taking relaxation into account

374 According to Equations 7-9, the stress in AAC by taking relaxation into account is calculated
 375 and shown in Figure 17. It can be seen that the calculation considering the elastic part of the
 376 autogenous shrinkage and the relaxation of the stress with time provides a fairly good
 377 agreement between calculated and measured stress evolutions in AAC. . For AAS concrete,
 378 the calculation underestimates the stress in the first 7 days while overestimates the stress at
 379 20 days. For AASF concrete, an opposite trend is observed. This discrepancy is probably
 380 because these two concrete mixtures have different creep compliances, but in the calculation,
 381 the same model was used.

382 In Equations 4-6, the water-to-solid ratio and the reaction degree were considered for the
 383 creep calculation of the paste, however, the creep behaviour of concrete depends not only on
 384 the deformability of the paste but also on the restraining effect of the aggregates. The
 385 restraining effect of aggregates is determined not only by the size and volume fraction of the
 386 aggregates but also by the interface between paste and aggregates, viz. the interfacial
 387 transition zone (ITZ) [62,63]. In this study, the size and the volume fraction of aggregates for
 388 AAS and AASF concrete are the same (see Table 2), however, differences in the ITZ properties
 389 of AAS concrete and AASF concrete were found in previous studies [48,54] which investigated
 390 the same mixtures as this study. Generally, AASF concrete has more porous and weaker ITZ
 391 than AAS concrete [48,54]. Although the influence of ITZ on the deformation of concrete has
 392 not been clearly understood [64–66], it has been found that the creep of the ITZ is higher
 393 compared to the bulk matrix [67]. Therefore, the creep compliance of AASF concrete is
 394 supposed to be less restrained by the aggregates due to the weaker ITZ. As a result, using the

395 same equations and empirical parameters in calculation may lead to slight overestimation and
396 underestimation of the creep in AAS and AASF concrete, respectively.



397

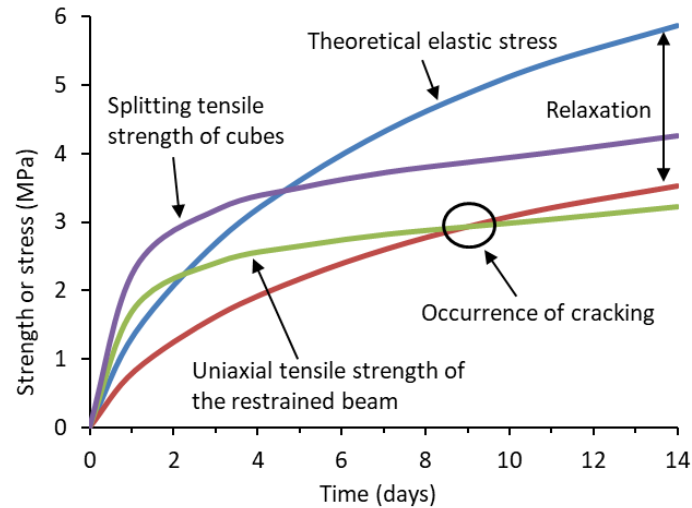
398 Figure 17. Calculated stress in AAS (a) and AASF (b) concrete from the elastic part of the autogenous shrinkage
399 and the elastic modulus of the concrete, with the stress relaxation taken into account.

400

401 Despite the reason for the small discrepancies exhibited in Figure 17, the calculations in this
402 section have clearly shown the important roles played by relaxation in the stress evolution of
403 restrained AAC. Neglecting the creep and relaxation behaviour would lead to an
404 overestimation of the self-induced stress in AAC.

405 4.4 Estimation of the cracking initiation of AAC

406 With the calculated stress and tensile strength, the cracking initiation of the concrete can be
407 estimated. Due to the difficulty in conducting the uniaxial tensile test on concrete, the tensile
408 strength measured by the splitting test on concrete cubes or cylinders is usually used to
409 estimate the cracking potential [68]. However, it should be noted that the maximum stress of
410 concrete at failure is normally lower than the splitting tensile strength. The first reason is that
411 the tensile strength of concrete measured uniaxially is normally lower than the tensile
412 strength measured by splitting tests [69]. The second reason is the reducing effect of
413 relaxation on the tensile strength. While the relaxation can reduce the stress, it can also
414 aggravate the development of microcracking, which is detrimental to the tensile strength
415 [70,71]. Due to the local creep, viz. change of the internal geometric constitution of the paste,
416 the internal stress is redistributed with time, causing a relief of stress in higher stressed zones
417 but new stress concentration in other zones [35]. As a result, additional local failure within the
418 concrete can be induced. This is probably the reason why the tensile strength of concrete
419 which experiences creep/relaxation under restrained condition is normally lower than that of
420 concrete which is free from loading [70,72]. Therefore, the influence of relaxation on the
421 tensile strength needs also a consideration when estimating the cracking time of the concrete.
422 The third reason is that the cube under splitting stress has to fail in the middle, while the beam
423 under uniaxial tensile stress will fail at the weakest cross-section. Due to the larger size of the
424 beam than the cube, the tensile strength of the weakest cross-section should be statistically
425 lower than that of the middle cross-section of the cube. Hence, a reduced tensile strength is
426 normally considered, as shown in Figure 18.



427

428 Figure 18. A schematic diagram of the stress development and the resultant cracking of concrete due to
 429 restrained shrinkage.

430

431 For OPC based concrete, the failure stress-to-splitting strength ratios were in the range of 0.7
 432 - 0.8 [35,73,74]. Based on experiments on a dozen specimens, Lokhorst [35] found OPC based
 433 concrete, on average, failed at 75% of the actual tensile splitting strength irrespective of the
 434 age. However, the failure stress-to-splitting strength ratios for AAS concrete and AASF
 435 concrete in this study were only 0.56 and 0.37, respectively. These ratios were lower than
 436 those for OPC concretes, possibly because of the more evident creep/relaxation in AAC.
 437 Besides, it should be noted that only a limited number of samples were tested in this study.
 438 To obtain a representative reduced factor of the tensile strength of AAC, intensive
 439 experimental work on numerous samples and mixtures is needed.

440 5. Concluding remarks

441 In this study, the cracking potential of AAS and AASF concrete subjected to restrained
 442 autogenous shrinkage is evaluated. Based on the experimental and numerical results, the
 443 following remarks can be made:

- 444 1. AAC concrete shows generally high compressive strength. The $f_{t,sp}/f_c$ and the elastic
 445 modulus of AAC decrease with the curing age, which may be due to the development
 446 of microcracking resulting from the continuous autogenous shrinkage.
- 447 2. TSTM is utilized for the first time to track the stress evolution and cracking initiation of
 448 AAC. AAC is found to show moderate-low cracking potential, despite its high
 449 autogenous shrinkage. The low autogenous shrinkage-induced stress in AAC is mainly
 450 attributed to the pronounced relaxation of the concrete.
- 451 3. With the elastic part of the autogenous shrinkage and the stress relaxation taken into
 452 account, a very good prediction of the stress evolution in AAC is obtained. In contrast,
 453 calculations without considering the creep and relaxation would lead to a significant
 454 overestimation of the stress in AAC.

455 4. A reducing factor of the splitting tensile strength needs to be considered when
456 estimating the cracking time of AAC, since the failure stress of the restrained concrete
457 beam is lower than the splitting tensile strength of cubes that are free from load.

458

459 Acknowledgment

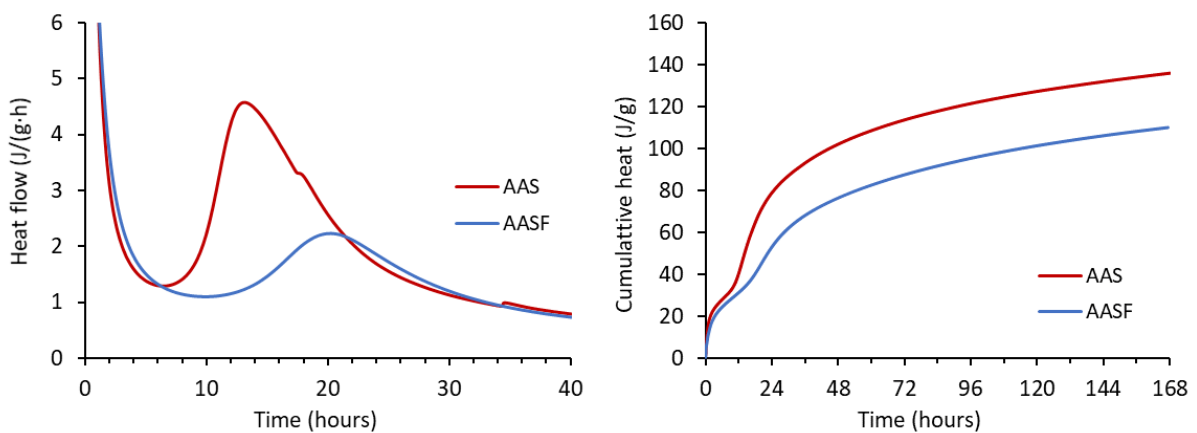
460 Zhenming Li and Xuhui Liang would like to acknowledge the funding supported by the China
461 Scholarship Council (CSC) under grant No. 201506120072 and No. 201806050051. This work
462 is supported also by the grant from the Netherlands Organisation for Scientific Research
463 (NWO). Prof. Klaas van Breugel is acknowledged for the discussion on the model. The two
464 anonymous reviewers are appreciated for their few but valuable comments.

465

466 Appendix A

467 In section 3.4, $Q(t)$ and Q_{max} of AAC was used to calculate the reaction degree and the creep
468 coefficient.

469 In this study, a TAM Air isothermal calorimeter (Thermometric) was used to measure the
470 reaction heat of the pastes. Before measurements, the calorimeter was calibrated at 20 °C.
471 The temperature of the measuring channels of the calorimeter was controlled at 20 ± 0.01 °C.
472 Approximately 5 g of paste were cast into each glass vial and were immediately loaded into
473 the measuring channels. The internal diameter of the glass vial was 24.5 mm. The mixing and
474 loading procedures lasted about 15min from the moment of adding activator. The data was
475 recorded every 1 min to 7 days. The calorimetry results were normalized by the weight of the
476 paste. The heat flow of the paste is shown in Figure A.1 (a) and the $Q(t)$ of AAS and AASF
477 pastes during the first week of reaction was shown in Figure A.1 (b). Due to the same curing
478 condition (iso-thermal) of the paste and concrete samples, the reaction degrees of the paste
479 and the concrete are assumed identical at all time.



480

481

Figure A.1. Reaction heat of AAS and AASF pastes.

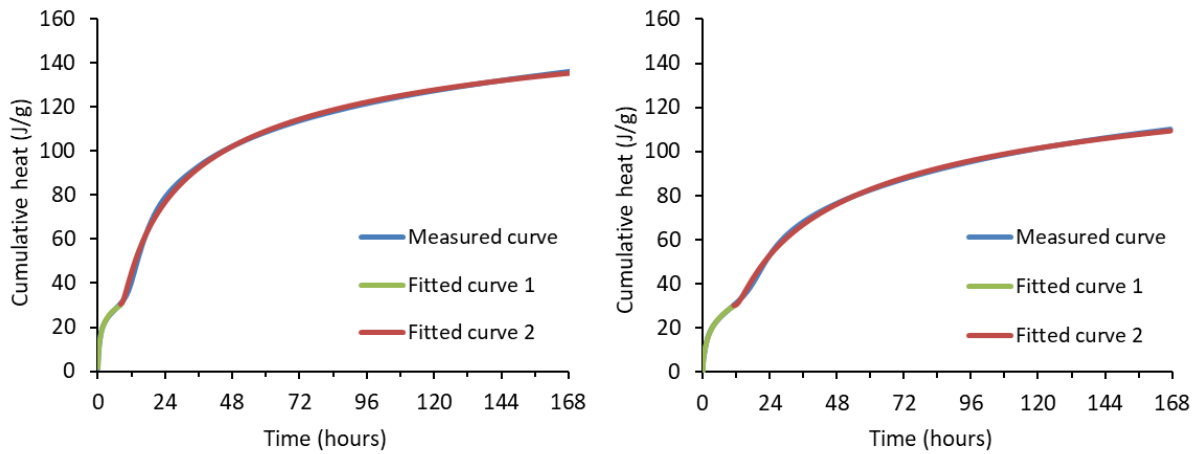
482

483 For the $Q(t)$ after the first week and the Q_{max} of the paste/concrete, the method of curve
 484 fitting is needed. According to [44,75,76], the exponential model shown in Equation A.1 can
 485 provide a good Q_{max} prediction for AAMs.

$$486 \quad Q(t) = Q_{max} \exp\left[-\left(\frac{\tau}{t}\right)^\beta\right] \quad (A.1)$$

487 where τ and β are the fitting parameters associated with the time and the shape of the
 488 exponential model.

489 Due to the inability of Equation A.1 to fit multi-curvature evolutions, a piecewise
 490 approximation by two functions is needed for the fitting of the heat flow curves of AAMs
 491 paste. The fitted curves of the heat flow of AAS and AASF pastes are presented in Figure A.2,
 492 in comparison with the experimental data. The fitting parameters and the accuracy of the
 493 fitting (indicated by the adjusted R-square) are shown in Table A.1.



494

495 Figure A.2. Fitted heat flow of AAS paste (a) and AASF paste (b), in comparison with the experimentally
 496 measured heat flow.

497

498 Table A.1. Fitted parameters of the exponential model for the heat flow of AAS and AASF paste.

Mixtures	Q_{max}	τ	β	R-square
AAS curve 1	-	1.98	0.33	0.998
AAS curve 2	155.04	23.68	0.49	0.998
AASF curve 1	-	44.02	0.22	0.999
AASF curve 2	139.13	46.04	0.47	0.999

499

500 Figure A.2 and Table A.1 indicate a very good fitting of the curves. It can be seen in Table A.1
 501 that AAS paste has a higher Q_{max} than AASF paste, which is reasonable. With the fitted
 502 parameters, the $Q(t)$ and the reaction degree α of AAS and AASF concrete at different curing
 503 ages can be then calculated, as shown in Table A.2. The results were used to in section 3.4 to
 504 calculate the creep coefficient.

505 Table A.2. $Q(t)$ and α of AAS and AASF concrete at different ages.

AAS concrete	8h	1d	2d	3d	7d	14d	20d
$Q(t)$	30.53	78.90	102.09	113.70	135.98	148.63	153.70
α	0.20	0.51	0.66	0.73	0.88	0.96	0.99
AASF concrete	11h	1d	2d	3d	7d	16.6d	-
$Q(t)$	29.77	53.67	77.03	88.11	110.65	127.00	-
α	0.19	0.39	0.55	0.63	0.80	0.91	-

506

507 Reference

- 508 [1] G. Habert, C. Ouellet-Plamondon, Recent update on the environmental impact of
509 geopolymers, RILEM Tech. Lett. 1 (2016) 17–23.
- 510 [2] J.L. Provis, S. a Bernal, Geopolymers and Related Alkali-Activated Materials, Annu. Rev.
511 Mater. Res. 44 (2014) 299–327. doi:doi:10.1146/annurev-matsci-070813-113515.
- 512 [3] J.L. Provis, Alkali-activated materials, Cem. Concr. Res. 114 (2018) 40–48.
513 doi:10.1016/j.cemconres.2017.02.009.
- 514 [4] C. Shi, A.F. Jiménez, A. Palomo, New cements for the 21st century: The pursuit of an
515 alternative to Portland cement, Cem. Concr. Res. 41 (2011) 750–763.
516 doi:10.1016/j.cemconres.2011.03.016.
- 517 [5] ASTM C618 - 19, Standard specification for coal fly ash and raw or calcined natural
518 pozzolan for use in concrete, (2008). doi:10.1520/C0618-19.2.
- 519 [6] N. Gamage, K. Liyanage, S. Fragomeni, S. Setunge, Overview of different types of fly ash
520 and their use as a building and construction material, (2013).
- 521 [7] J.L. Provis, Activating solution chemistry for geopolymers, in: Geopolymers, Elsevier,
522 2009: pp. 50–71.
- 523 [8] F. Collins, J.G. Sanjayan, Early age strength and workability of slag pastes activated by
524 NaOH and Na₂CO₃, Cem. Concr. Res. 28 (1998) 655–664.
- 525 [9] H. Tan, X. Deng, X. He, J. Zhang, X. Zhang, Y. Su, J. Yang, Compressive strength and
526 hydration process of wet-grinded granulated blast-furnace slag activated by sodium
527 sulfate and sodium carbonate, Cem. Concr. Compos. 97 (2019) 387–398.
528 doi:https://doi.org/10.1016/j.cemconcomp.2019.01.012.
- 529 [10] J.L. Provis, J.S.J. Van Deventer, Alkali Activated Materials, 2014. doi:10.1007/978-94-
530 007-7672-2.
- 531 [11] B.S. Gebregziabihier, R.J. Thomas, S. Peethamparan, Temperature and activator effect
532 on early-age reaction kinetics of alkali-activated slag binders, Constr. Build. Mater. 113
533 (2016) 783–793. doi:10.1016/j.conbuildmat.2016.03.098.
- 534 [12] M. Ben Haha, G. Le Saout, F. Winnefeld, B. Lothenbach, Influence of activator type on
535 hydration kinetics, hydrate assemblage and microstructural development of alkali
536 activated blast-furnace slags, Cem. Concr. Res. 41 (2011) 301–310.

- 537 doi:10.1016/j.cemconres.2010.11.016.
- 538 [13] F. Pacheco-Torgal, Z. Abdollahnejad, S. Miraldo, M. Kheradmand, Alkali-activated
539 cement-based binders (AACBs) as durable and cost-competitive low-CO₂ binder
540 materials: some shortcomings that need to be addressed, Butterworth-Heinemann,
541 Oxford, UK, 2017.
- 542 [14] F. Pacheco-Torgal, Z. Abdollahnejad, A.F. Camões, M. Jamshidi, Y. Ding, Durability of
543 alkali-activated binders: A clear advantage over Portland cement or an unproven issue?,
544 *Constr. Build. Mater.* 30 (2012) 400–405. doi:10.1016/j.conbuildmat.2011.12.017.
- 545 [15] M. Mastali, P. Kinnunen, A. Dalvand, R. Mohammadi Firouz, M. Illikainen, Drying
546 shrinkage in alkali-activated binders – A critical review, *Constr. Build. Mater.* 190 (2018)
547 533–550. doi:10.1016/j.conbuildmat.2018.09.125.
- 548 [16] J. Ma, F. Dehn, Shrinkage and creep behavior of an alkali-activated slag concrete, *Struct.*
549 *Concr.* 18 (2017) 801–810. doi:10.1002/suco.201600147.
- 550 [17] C. Cartwright, F. Rajabipour, A. Radli, Shrinkage Characteristics of Alkali-Activated Slag
551 Cements, *J. Mater. Civ. Eng.* 27 (2014) 1–9. doi:10.1061/(ASCE)MT.1943-5533.0001058.
- 552 [18] B.D. Kumarappa, S. Peethamparan, M. Ngami, Autogenous shrinkage of alkali activated
553 slag mortars: Basic mechanisms and mitigation methods, *Cem. Concr. Res.* 109 (2018)
554 1–9. doi:10.1016/j.cemconres.2018.04.004.
- 555 [19] S. Uppalapati, Ö. Cizer, Assessing the autogenous shrinkage of alkali- activated slag/fly
556 ash mortar blends, *Am. Concr. Institute, ACI Spec. Publ.* 2017-Janua (2017).
- 557 [20] G. Fang, W. Tu, Y. Zhu, M. Zhang, AUTOGENOUS SHRINKAGE OF ALKALI-ACTIVATED FLY
558 ASH-SLAG PASTES WITH AND WITHOUT SAP, in: 4th Int. Conf. Serv. Life Des.
559 Infrastructures, 2018: pp. 449–455.
- 560 [21] M. Nedeljković, Z. Li, G. Ye, Setting, Strength, and Autogenous Shrinkage of Alkali-
561 Activated Fly Ash and Slag Pastes: Effect of Slag Content, *Materials (Basel)*. 11 (2018)
562 2121. doi:10.3390/ma11112121.
- 563 [22] Z. Li, S. Zhang, X. Liang, G. Ye, Internal curing of alkali-activated slag-fly ash paste with
564 superabsorbent polymers, *Constr. Build. Mater.* (2020) (under review).
- 565 [23] Z. Li, M. Wyrzykowski, H. Dong, J. Granja, M. Azenha, P. Lura, G. Ye, Internal curing by
566 superabsorbent polymers in alkali-activated slag, *Cem. Concr. Res.* 135 (2020) 106123.
567 doi:10.1016/j.cemconres.2020.106123.
- 568 [24] Z. Li, M. Nedeljkovic, Y. Zuo, G. Ye, Autogenous shrinkage of alkali-activated slag-fly ash
569 pastes, in: 5th Int. Slag Valor. Symp., Leuven, 2017: pp. 369–372.
- 570 [25] T. Lu, Z. Li, H. Huang, Effect of Supplementary Materials on the Autogenous Shrinkage
571 of Cement Paste, *Materials (Basel)*. 13 (2020) 3367.
- 572 [26] A.M. Neville, *Properties of Concrete*, 2011.
- 573 [27] E. Tazawa, *Autogenous shrinkage of concrete*, CRC Press, 1998.
- 574 [28] M.S. Sule, *Effect of reinforcement on early-age cracking in high strength concrete*, Delft
575 University of Technology, 2003.
- 576 [29] P. Lura, *Autogenous Deformation and Internal Curing of Concrete*, Delft University of

- 577 Technology, 2003.
- 578 [30] Z. Li, A. Kostiuchenko, G. Ye, Autogenous shrinkage-induced stress of alkali-activated
579 slag and fly ash concrete under restraint condition, in: ECI (Ed.), Alkali Act. Mater.
580 Geopolymers Versatile Mater. Offer. High Perform. Low Emiss., Tomar, 2018: p. 24.
- 581 [31] S.I. Igarashi, A. Bentur, K. Kovler, Autogenous shrinkage and induced restraining
582 stresses in high-strength concretes, *Cem. Concr. Res.* 30 (2000) 1701–1707.
583 doi:10.1016/S0008-8846(00)00399-9.
- 584 [32] F. Collins, J.G. Sanjayan, cracking tendency of alkali-activated slag concrete subjected
585 to restrained shrinkage, *Cem. Concr. Res.* 30 (2000) 791–798. doi:10.1016/S0008-
586 8846(00)00243-X.
- 587 [33] NEN-EN 12390-3, Testing hardened concrete - Part 3: Compressive strength of test
588 specimens, (2009).
- 589 [34] B. Delsaute, C. Boulay, J. Granja, J. Carette, M. Azenha, C. Dumoulin, G. Karaiskos, A.
590 Deraemaeker, S. Staquet, Testing Concrete E-modulus at Very Early Ages Through
591 Several Techniques: An Inter-laboratory Comparison, *Strain.* (2016) 91–109.
592 doi:10.1111/str.12172.
- 593 [35] S.J. Lokhorst, Deformational behaviour of concrete influenced by hydration related
594 changes of the microstructure, Delft University of Technology, 2001.
- 595 [36] ASTM C 1581, Standard Test Method for Determining Age at Cracking and Induced
596 Tensile Stress Characteristics of Mortar and Concrete under Restrained Shrinkage,
597 *ASTM Int.* (2009) 1–7. doi:10.1520/C1581.
- 598 [37] Z. Li, T. Lu, X. Liang, H. Dong, J. Granja, M. Azenha, G. Ye, Mechanisms of autogenous
599 shrinkage of alkali-activated slag and fly ash pastes, *Cem. Concr. Res.* 135 (2020)
600 106107. doi:10.1016/j.cemconres.2020.106107.
- 601 [38] T. Lu, Autogenous shrinkage of early age cement paste and mortar, Delft University of
602 Technology, 2019.
- 603 [39] K. Van Breugel, Relaxation of young concrete, (1980) 144.
- 604 [40] Z.P. BAZANT, Prediction of concrete creep effects using age-adjusted effective modulus
605 method, *J. Am. Concr. Inst.* 69 (1972) 212–217.
- 606 [41] H. van der Ham, E. Koenders, K. van Breugel, Creep model uncertainties in early-age
607 concrete simulations, *Proc. Concreep.* 8 (2008) 431–436.
- 608 [42] K.A. Riding, J.L. Poole, K.J. Folliard, M.C.G. Juenger, A.K. Schindler, Modeling hydration
609 of cementitious systems, *ACI Mater. J.* 109 (2012) 225–234.
- 610 [43] A.K. Schindler, K.J. Folliard, Heat of hydration models for cementitious materials, *ACI*
611 *Mater. J.* 102 (2005) 24.
- 612 [44] D. Ravikumar, N. Neithalath, Reaction kinetics in sodium silicate powder and liquid
613 activated slag binders evaluated using isothermal calorimetry, *Thermochim. Acta.* 546
614 (2012) 32–43. doi:10.1016/j.tca.2012.07.010.
- 615 [45] F. Wittmann, Bestimmung physikalischer Eigenschaften des Zementsteins, 1974.
- 616 [46] NEN-EN 206-1, Concrete - Part 1: Specification, performance, production and

- 617 conformity, Eur. Comm. Stand. (2001).
- 618 [47] A. Fernández-Jiménez, J.G. Palomo, F. Puertas, Alkali-activated slag mortars:
619 mechanical strength behaviour, *Cem. Concr. Res.* 29 (1999) 1313–1321.
- 620 [48] M. Nedeljković, Carbonation mechanism of alkali-activated fly ash and slag materials:
621 In view of long-term performance predictions, Delft University of Technology, 2019.
- 622 [49] F. Puertas, S. Martínez-Ramírez, S. Alonso, T. Vázquez, Alkali-activated fly ash/slag
623 cements. Strength behaviour and hydration products, *Cem. Concr. Res.* 30 (2000) 1625–
624 1632. doi:10.1016/S0008-8846(00)00298-2.
- 625 [50] Y. Ma, Microstructure and Engineering Properties of Alkali Activated Fly Ash -as an
626 environment friendly alternative to Portland cement, 2013.
- 627 [51] Z. Yu, Microstructure Development and Transport Properties of Portland Cement-fly
628 Ash Binary Systems, 2015.
- 629 [52] N. Arioglu, Z. Canan Girgin, E. Arioglu, Evaluation of ratio between splitting tensile
630 strength and compressive strength for concretes up to 120 MPa and its application in
631 strength criterion, *ACI Mater. J.* 103 (2006) 18–24. doi:10.14359/15123.
- 632 [53] Z. Li, M. Nedeljković, B. Chen, G. Ye, Mitigating the autogenous shrinkage of alkali-
633 activated slag by metakaolin, *Cem. Concr. Res.* 122 (2019) 30–41.
634 doi:10.1016/j.cemconres.2019.04.016.
- 635 [54] S. Prinsse, D.A. Hordijk, G. Ye, P. Lagendijk, M. Luković, Time-dependent material
636 properties and reinforced beams behavior of two alkali-activated types of concrete,
637 *Struct. Concr.* 21 (2020) 642–658. doi:10.1002/suco.201900235.
- 638 [55] P. Lura, O.M. Jensen, J. Weiss, Cracking in cement paste induced by autogenous
639 shrinkage, *Mater. Struct.* 42 (2009) 1089–1099. doi:10.1617/s11527-008-9445-z.
- 640 [56] F. Collins, J.G. Sanjayan, Microcracking and strength development of alkali activated
641 slag concrete, *Cem. Concr. Compos.* 23 (2001) 345–352. doi:10.1016/S0958-
642 9465(01)00003-8.
- 643 [57] P. Lura, K. Van Breugel, I. Maruyama, Effect of curing temperature and type of cement
644 on early-age shrinkage of high-performance concrete, *Cem. Concr. Res.* 31 (2001)
645 1867–1872. doi:10.1016/S0008-8846(01)00601-9.
- 646 [58] A. Darquennes, S. Staquet, M.P. Delplancke-Ogletree, B. Espion, Effect of autogenous
647 deformation on the cracking risk of slag cement concretes, *Cem. Concr. Compos.* 33
648 (2011) 368–379. doi:10.1016/j.cemconcomp.2010.12.003.
- 649 [59] H. Ye, A. Radlińska, Shrinkage mechanisms of alkali-activated slag, *Cem. Concr. Res.* 88
650 (2016) 126–135. doi:10.1016/j.cemconres.2016.07.001.
- 651 [60] A. Kostiuchenko, J. Liu, Z. Aldin, Mechanical properties and creep behavior of an alkali-
652 activated concretemechanical properties and creep behavior of an alkali-activated
653 concrete, in: *Alkali Act. Mater. Geopolymers Versatile Mater. Offer. High Perform. Low*
654 *Emiss.*, 2018: p. 9.
- 655 [61] T.C. Hansen, Creep and stress relaxation of concrete: a theoretical and experimental
656 investigation, Svenska forskningsinstitutet för cement och betong vid Kungl. Tekniska
657 högskolan, 1960.

- 658 [62] R.L. Al-Mufti, A.N. Fried, Pulse velocity assessment of early age creep of concrete,
659 Constr. Build. Mater. 121 (2016) 622–628.
- 660 [63] O. Bernard, F.-J. Ulm, J.T. Germaine, Volume and deviator creep of calcium-leached
661 cement-based materials, Cem. Concr. Res. 33 (2003) 1127–1136.
- 662 [64] M. Briffaut, F. Benboudjema, C. Laborderie, J.-M. Torrenti, Creep consideration effect
663 on meso-scale modeling of concrete hydration process and consequences on the
664 mechanical behavior, J. Eng. Mech. 139 (2013) 1808–1817.
- 665 [65] C. Pichler, R. Lackner, A multiscale creep model as basis for simulation of early-age
666 concrete behavior, Comput. Concr. 5 (2008) 295–328.
- 667 [66] P. Lura, M. Wyrzykowski, Influence of Aggregate Restraint on Volume Changes:
668 Experiments and Modelling, in: Concreep, 2015: pp. 17–23.
669 doi:doi:10.1061/9780784479346.
- 670 [67] V. Zacharda, J. Němeček, H. Šimonová, B. Kucharczyková, M. Vyhlídal, Z. Keršner,
671 Influence of Interfacial Transition Zone on Local and Overall Fracture Response of
672 Cementitious Composites, in: Key Eng. Mater., 2018: pp. 97–102.
- 673 [68] NEN-EN 12390-3, Testing hardened concrete - Part 6: Tensile splitting strength of test
674 specimens, (2009).
- 675 [69] British Standards Institution, Eurocode 2: Design of concrete structures: Part 1-1:
676 General rules and rules for buildings, British Standards Institution, 2004.
- 677 [70] D.J. Cook, P. Chindaprasirt, Influence of loading history upon the tensile properties of
678 concrete, Mag. Concr. Res. 33 (1981) 154–160. doi:10.1680/mac.1981.33.116.154.
- 679 [71] A.D. Ross, Creep of concrete under variable stress, in: J. Proc., 1958: pp. 739–758.
- 680 [72] D.J. Cook, P. Chindaprasirt, Influence of loading history upon the compressive
681 properties of concrete, Mag. Concr. Res. 32 (1980) 89–100.
- 682 [73] H.G. Heilmann, H. Hilsdorf, K. Finsterwalder, Strength and Deformation of Concrete
683 Under Tensile Stress, Bulletin. (1969) 94.
- 684 [74] J. Byfors, Plain concrete at early ages, Cement-och betonginst., 1980.
- 685 [75] S. Chithiraputhiran, N. Neithalath, Isothermal reaction kinetics and temperature
686 dependence of alkali activation of slag, fly ash and their blends, Constr. Build. Mater.
687 45 (2013) 233–242. doi:10.1016/J.CONBUILDMAT.2013.03.061.
- 688 [76] S. Zhang, Y. Zuo, Z. Li, G. Ye, Isothermal calorimetric study on heat evolution and
689 apparent activation energy of alkali-activated slag/fly ash paste, in: 2nd Int. Conf.
690 Sustain. Build. Mater., Eindhoven, 2019: pp. 1–8.

691